UV-enabled Defect Engineering in Multilayer GaSe and InSe and UV Writing of Grating Pattern

Bhojraj Bhandari,[1#] Sinto Varghese,[1#] Amar R. Ghimire,[1] Bimal Neupane,[1] Sicheng Wang,[2] Yan Jiang,[1] Roberto Gonzalez Rodriguez,[1] Sergiy Krylyuk,[3] Albert V. Davydov,[3] Yuanxi Wang,[1] Hao Yan,[2] Jingbiao Cui,[1] and Yuankun Lin,[1,4*]

[1]*Department of Physics, University of North Texas, Denton, TX 76203, USA*

[2]*Department of Chemistry, University of North Texas, Denton, TX 76203, USA*

[3]*Materials Science and Engineering Division, National Institute of Standards and Technology (NIST), Gaithersburg, MD 20899, USA*

[4]*Department of Electrical Engineering, University of North Texas, Denton, TX 76203, USA*

# equal contributions

*****Correspondence**:** yuankun.lin@unt.edu

Abstract

III-VI post-transition metal chalcogenides are layered semiconductor materials that exhibit direct band gaps in multilayers. Defect engineering is essential in 2D layered semiconductors for functional devices. Here, we report defect engineering in multilayer gallium selenide (GaSe) and indium selenide (InSe), where defects generated by ultraviolet (UV, 325 nm) laser irradiation result in an additional photoluminescence (PL) line. The additional PL line is due to defect-bound excitons. Characteristics of the defect emission are similar in GaSe and InSe samples subjected to UV-irradiation, air annealing, or hydrostatic pressure. Two-beam UV interference was applied to create grating patterns with a periodic array of low and high densities of defects in GaSe. Density functional theory has identified the defect type in GaSe. The results provide valuable insights into defect generation and UV scribe of photonic circuits in 2D Se-based multi-layers for optical integration in a 2D platform.

Keywords: Defect Engineering, grating fabrication, 2D multilayered materials, photoluminescence, exciton, density functional theory, thermal annealing, UV-irradiation, fluorescence lifetime, GaSe, InSe.

Introduction:

2D layered materials such as metal oxides, black phosphorus (BP),[1,2] and transition metal dichalcogenides, e.g., MoS_2, $MoSe_2$, WS_2, and WSe_2 [3–5] have emerged as exciting candidates for nano-scale applications. Another promising class of 2D materials for next-generation electronic applications is Group-III monochalcogenides (MX, with M being Ga or In and X being a chalcogen such as S, Se, and Te).[6–10] In the case of gallium selenide (GaSe) and indium selenide (InSe), a monolayer consists of two Ga or In atoms and two Se atoms arranged as Se-Ga-Ga-Se and Se-In-In-Se, as shown in Figure S1(a, b) in the Supporting Information. In the bulk form, InSe and GaSe have direct band gaps that can be tuned by layer thickness, as demonstrated both theoretically [11–13] and experimentally[10,14,15] or by external stimuli, e.g., mechanical deformation.[10,16,17] Their ability to withstand large deformations without breakdown is an exciting property to be used for flexible electronic devices and strain engineering applications.[18,19]

GaSe has excellent optoelectronic characteristics for second-order optical nonlinearity, single-photon emission, and terahertz applications.[20–24] Similarly, InSe is another promising 2D material that exhibits exceptional electron mobility and ultrahigh photo-response, making it useful for computing, field effect transistors, and gas sensors.[3,14,25–28] An effective way to dynamically modify the electronic band structure and enhance the optical properties of 2D layered materials is through defect engineering. [29–33] In particular, point defects in GaSe and InSe have been used and characterized as single-photon emitters.[20,34,35]

In general, lasers have been used for the fabrication of photonic devices, especially the Bragg grating in optical fiber.[36] Laser direct writing can provide a fast patterning of photonic devices over a large area or volume.[37,38] Optical methods for defect engineering in 2D materials are very attractive due to relatively easy implementation and low cost. The ultra-fast laser[39] and the ultraviolet (UV) lamp[40] have successfully been used to generate defects in h-BN and MoS_2, respectively, for single-photon emitters. UV 325 nm and 266 nm lasers were used to generate stable defects in multi-layer MoS_2 and GaSe.[41,42] In this work, we explored the use of a 325 nm He-Cd laser for the defect engineering in GaSe and InSe. We observe an additional defect-related photoluminescence (PL) emission in the UV-irradiated multilayer GaSe and InSe that remains stable in Al_2O_3-capped samples. The two-beam interference of a coherent 325 nm laser was able to generate grating patterns in 2D multi-layer GaSe, opening a path toward UV laser writing of optical circuits on a 2D platform.

Methods:

Crystal Growth and characterization: GaSe and InSe single crystals were grown by the vertical Bridgman method using pre-synthesized polycrystalline materials. The charge was vacuum sealed in a graphitized quartz ampule. The melt was maintained at 990 °C for GaSe and 720 °C for InSe for several hours before the ampule was moved across a temperature gradient at a 0.5 mm/h rate. The ε-phase of GaSe and the γ-phase of InSe were confirmed by X-ray diffraction and transmission electron microscopy measurements.

Creating Defects in Multilayer GaSe and InSe using 325 nm UV Laser irradiation: The GaSe and InSe samples were mechanically exfoliated using Scotch and thermal release tapes. A freshly cleaved layered bulk crystal on thermal release tape is placed onto a 270 nm-thick SiO_2-coated silicon wafer using a polydimethylsiloxane (PDMS) stamp, and gentle pressure is applied to ensure good contact between the crystal and the substrate. Thermal release tape was then removed by heating to 100 °C. The prepared sample was protected with 30 nm Al_2O_3 using atomic layer deposition (ALD). The thickness of the flakes was measured by a profilometer. The GaSe and InSe samples were irradiated for different durations with a continuous-wave He-Cd UV 325 nm laser (IK3301R-G, 200 mW) through an optical microscopic objective in air. Defects in GaSe multi-layers were also generated by exposing them to the two-beam interference pattern of a UV 325 nm laser.

Creating Defects in Multilayer GaSe and InSe through Thermal Annealing: To create the defects by thermal annealing, we followed the processes from exfoliation to ALD, as mentioned in the section above. GaSe and InSe samples were annealed at 150 °C on a hot plate in ambient air conditions for 3 h, followed by rapid cooling inside a fridge at 0 °C for 3 min.[43]

Photoluminescence and Raman Measurements: The PL and Raman measurements were performed at room and low temperatures using a Renishaw inVia Raman microscope setup with a 532 nm laser excitation and 1800 lines mm^{-1} and 1200 lines mm^{-1} gratings for GaSe and InSe, respectively. All the Raman and PL measurements were taken from the same region of the samples, maintained under the same experimental conditions. A 50x objective lens having numerical

aperture (NA) = 0.5 was used for all measurements. The Linkam THMS600 stage was mounted on the microscope system for low- and room-temperature measurements. Precise adjustments of the incident laser power were achieved using a combination of neutral density filters and laser power control software provided by Cobolt Samba. The exposure time was consistently set at 10 s. Notably; 1 mW of laser power corresponded to a laser intensity of 0.59 kW/cm² in our optical setup. Therefore, we will document our results using laser power instead of laser intensity.

Fluorescence Lifetime Imaging (FLIM): A Micro Time 200 time-resolved confocal fluorescence microscope was used to obtain the FLIM images, decay curves, and lifetime histograms for laser-irradiated and GaSe multilayer samples. A picosecond 409 nm laser was used for the excitation of PL. The confocal microscope used a 40× objective lens (numerical aperture NA = 0.4) with a working distance of 12.0 mm to reduce the height variation effect during the lifetime mapping. Data acquisition and analysis were carried out using the SymPho-Time 64 software. Bandpass filters 620 nm ± 5 nm (i.e., from 615 nm to 625 nm) and 650 nm ± 20 nm (i.e., from 630 nm to 670 nm) were used for free-exciton and for defect emission, respectively.

Profilometer Measurements: A FILMETRICS Profilm 3D Profilometer with white Light Interferometry (WLI) was used to measure the sample height profile. The envelope peak measurement parameter was selected under the 'single' tab in the WLI setting to characterize the surface profiles.

High-pressure method: High-pressure studies were carried out using a symmetric diamond anvil cell (DAC) by Almax Easylab, equipped with two Type-IIa diamond anvils with 600 μm culets. The layer samples are loaded into a 400 μm diameter hole, which is drilled into a 304 stainless steel gasket that has been pre-indented to a thickness of 60 μm. Pressure determination is achieved through ruby fluorescence measurements (BETSA). Silicone oil (Sigma Aldrich) is employed as the pressure-transmitting medium to provide hydrostatic pressure.

Computational Details: To model electronic structures, we employed density functional theory (DFT) using the Perdew-Burke-Ernzerhof (PBE) parametrization of the generalized gradient approximation (GGA) exchange-correlation functional,[44] with simulations performed in the Vienna Ab Initio Simulation Package (VASP).[45,46] The interaction between valence electrons and

ionic cores was modeled with projector-augmented wave (PAW) pseudo-potentials. [47,48] All defects were modeled within a 7×7×1 supercell of ε-GaSe, where convergence with respect to supercell size towards the dilute defect limit has reduced defect-defect interactions between periodic images to the degree that defect level dispersion is within 0.05 eV; this also corresponds to a defect concentration of 0.5 %. A plane-wave cutoff energy of 500 eV was applied, with the electronic convergence criterion set to 0.01 meV, and force relaxed to a threshold of 0.02 eV/Å. Spin-polarized calculations were systematically performed to determine the ground state of each defect: we considered local magnetic moments of 0 and 2 μ_B for V_{Se}, where the non-polarized 0 μ_B case was the ground state; we considered 1 and 3 μ_B for V_{Ga}, where 1 μ_B was the ground state. The Python library Pyprocar[49,50] and matplotlib[51] were used to plot all the band structures.

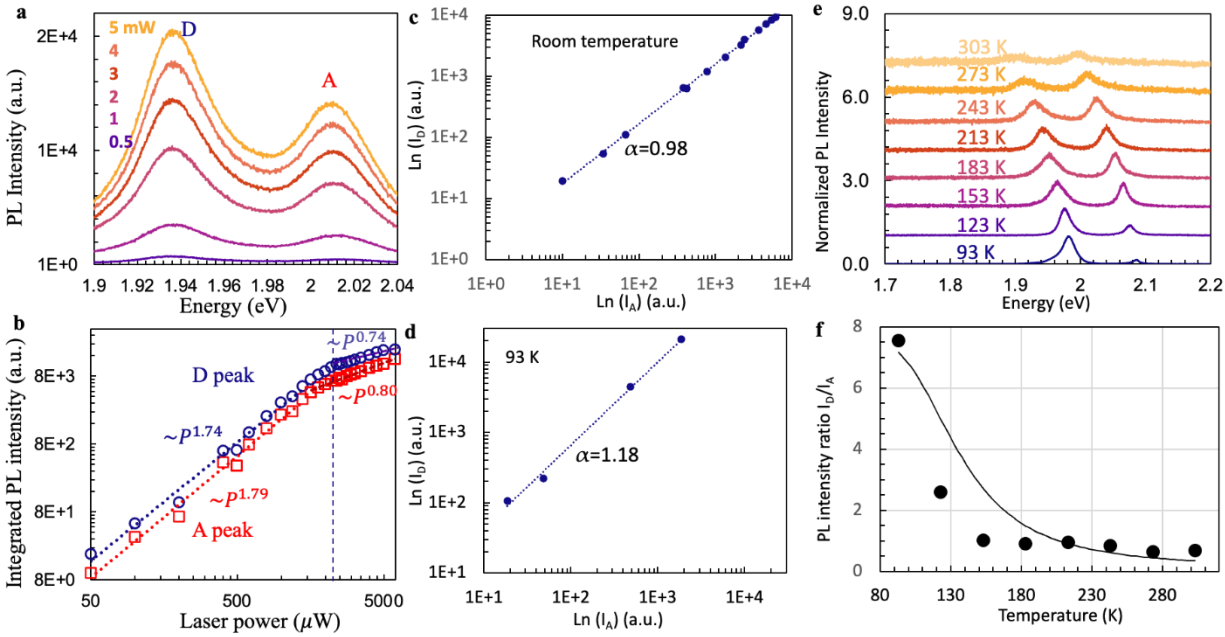

Figure 1 (a) PL spectra measured from UV irradiated multilayer GaSe sample under the laser power 0.5, 1, 2, 3, 4 and 5 mW, and (b) PL intensities of A peak (red squares) and D peak (blue circles) as a function of laser power. Logarithmic plot of D peak intensity as a function of A peak intensity at room temperature (c) and 93 K (d). Lines are power-law fits. (e) PL spectra from UV irradiated multilayer GaSe sample at different temperatures, and (f) the intensity ratio of D peak over A peak, I_D/I_A, as a function of temperature and its fit.

Results and Discussion

Defects Induced by UV Laser Irradiation in Multilayer GaSe and InSe

We prepared a multilayer GaSe with a thickness of 250 nm, as shown in Figure S2, coated with 30 nm of Al_2O_3. Figure S2c shows its Raman spectra, having two out-of-plane phonon modes $A_1'(1)$ at 133 cm^{-1} and $A_1'(2)$ at 306 cm^{-1}, and one in-plane mode $E''(2)$ at 212 cm^{-1}. [52] The sample was exposed to a UV 325 nm laser for 1 h. We measured the PL of the irradiated GaSe sample under excitation power from 0.1 to 5 mW at room temperature. Figure 1a shows the representative PL spectra under different laser excitation powers. We observe both an A peak around 2.019 eV, and a D peak at around 1.936 eV. The A peak corresponds to the free exciton emission, while the D peak at lower energy is attributed to defect emission associated with selenium vacancies (V_{se}), consistent with earlier reports on GaSe and related chalcogenides. [53–55] Figure 1b shows the PL intensity of free exciton (red diamonds) and defect emission (blue circles) peaks as a function of the excitation laser power. Below 1800 μW, the A and D peaks fit power-law exponents of 1.79 and 1.74, respectively, indicating superlinear increases in PL intensity. The intensity increase becomes sublinear at higher excitations, with the exponent values of 0.8 and 0.74 for the A and D peaks, respectively. The observed power-law exponents show the recombination dynamics in GaSe. The superlinear trend at low excitation power indicates efficient radiative processes, while the sublinear behavior at higher powers reflects defect saturation and enhanced nonradiative recombination.[56]

Under 532 nm laser illumination, the intensity of the free exciton peak in GaSe drops with increasing laser power above 3 mW.[57] The laser exposure time- and laser power-related PL intensity fluctuation in InSe has also been reported by another group.[58] To minimize additional laser-induced sample degradation during measurements, as well as to reduce PL fluctuations and background noise, we plotted the defect PL intensity as a function of A peak (exciton) intensity at excitation powers below 2000 μW at room temperature in Figure 1c and at 93 K in Figure 1d. [59,60] These two plots can be fitted by a power law $I_D \sim (I_A)^{\alpha}$ with $\alpha = 0.98$ at room temperature and $\alpha = 1.18$ at 93 K. For WS_2 and MoS_2, the exponent α is between 0.9 and 1.4, and a smaller value ($\alpha<1.5$) indicates an exciton bound to defects.[59–62] The exponent α for GaSe is between 0.98 and 1.18, compared with 1.09 in WS_2.[60] We can assume that the D peak in GaSe is due to the defect-bound exciton. To find the thermal activation energy, we measured the PL of GaSe at different

temperatures as shown in Figure 1e. The intensity ratio of D peak over A peak, I_D/I_A, as a function of temperature is shown in Figure 1f. The ratio I_D/I_A increases up to 7.6 when the temperature is below 180 K. At low temperatures, excitons are less likely to escape these localized states due to low thermal energy, resulting in a high population of defect-bound excitons. The relationship of I_D to I_A [60] could be described by

$$I_D \approx \frac{I_A}{a+b\ exp^{-\frac{E}{k_B T}}} \quad (1)$$

The fitting in Figure 1f gives the thermal activation energy E = 0.066 eV, corresponding to the separation energy of A and D peaks of 0.08 eV in Figure 1a and 0.10 eV in Figure 1e. If we only consider the data at 93 K and 303 K in Figure 1f, the fitting passing these two data points gives the thermal activation energy E=0.074 eV, closer to the experimental value than 0.066 eV.

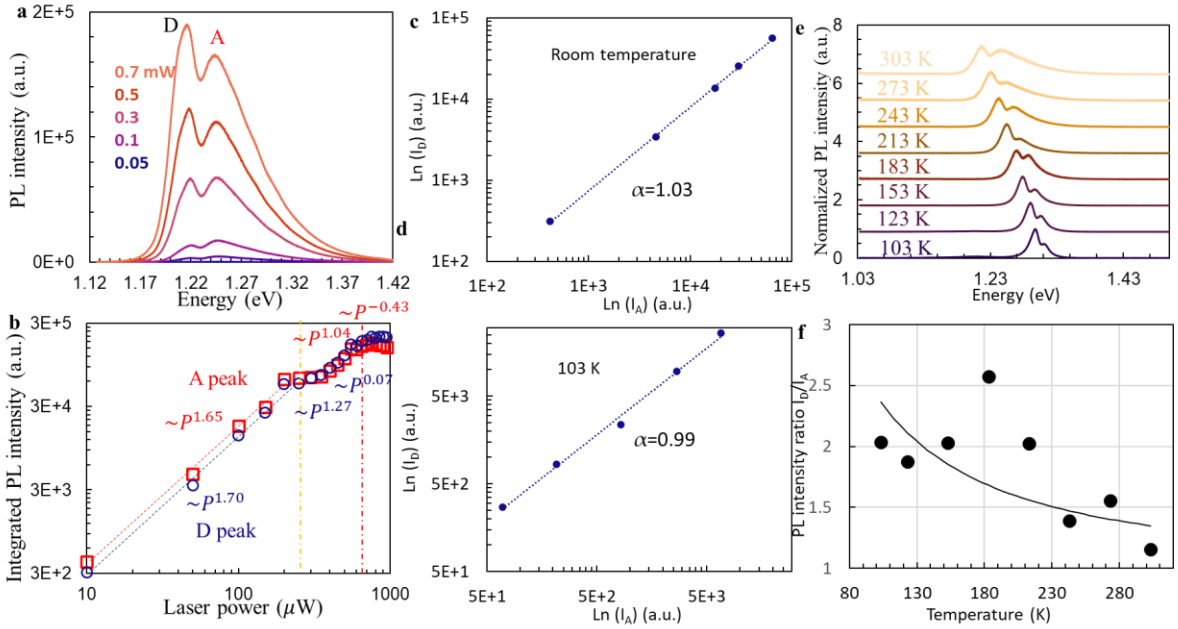

Figure 2 (a) PL spectra of UV irradiated InSe under the laser power 0.05, 0.1, 0.3, 0.5 and 0.7 mW, and (b) PL intensities of A peak (red squares) and D peak (blue circles) as a function of laser power. Logarithmic plot of D peak intensity as a function of A peak intensity at room temperature (c) and 103 K (d). Lines are power-law fits. (e) PL spectra from UV irradiated multilayer InSe sample at different temperatures, and (f) the intensity ratio of D peak over A peak, I_D/I_A, as a function of temperature and its fit.

Next, we study a multilayer InSe sample with a thickness of 270 nm passivated with 30 nm of Al_2O_3. The height profile and Raman spectrum of the sample are shown in Figure S3.[63] The sample was exposed to UV 325 nm laser irradiation for 5 min. Immediately after the UV irradiation, a D peak at around 1.21 eV, is observed together with the A peak (Figure 2a). Figures 2a and 2b show the representative PL spectra under different laser excitation powers and their PL intensity of free exciton (red squares) and defect emission (blue circles) peaks as a function of the excitation laser power. Below 250 μW, we fitted A peak and D peak to the power-law relationship $I \sim P^{1.65}$ and $I \sim P^{1.70}$, respectively, indicating a superlinear increase of A and D peak intensities with the excitation laser power. Those power-law relationships in InSe are very close to $I \sim P^{1.79}$ and $I \sim P^{1.74}$ in GaSe. Above 250 μW and below 600 μW, we fitted A peak and D peak to the power-law relationship $I \sim P^{1.04}$ and $I \sim P^{1.27}$. Above 600 μW, intensities of the two peaks essentially saturate. To minimize the laser power-related PL fluctuation effect,[58] we again plot the defect PL intensity as a function of A peak (exciton) intensity below 250 μW at room temperature in Figure 2c and at 103 K in Figure 2d.[59,60] The exponent of the power law $I_D \sim (I_A)^{\alpha}$ is 1.03 at room temperature and 0.99 at 103 K, indicating that the D peak is also due to a defect-bound exciton.[59–62] We also measured the PL of irradiated InSe at different temperatures as shown in Figure 2e and plotted their intensity ratio in Figure 2f. By fitting the data in Figure 2f with the equation (1), we obtained the thermal activation energy of 14 meV, compared with the bound-exciton binding energy of 14 meV at 103 K and 39 meV at 303 K in Figure 2e and of 26-29 meV in Figure 2a. The data points at 183 and 213 K deviate significantly from the fitting, probably due to the PL fluctuation with laser exposure time during PL measurement.[58] If we only consider the data at 103 K and 303 K in Figure 2f, the fitting passing these two data points gives the thermal activation energy E=12.5 meV, slightly smaller than the fitted value of 14 meV for the whole data points. Our experimental data shows that InSe[58] is much easier to generate defects by UV irradiation, and much more prone to laser power-related sample degradation than GaSe, that might be related to its smaller thermal activation energy compared to GaSe. It took 60 min and 5 min to generate defects in GaSe and InSe under 325 nm laser exposure, respectively.

Defect generation in GaSe and InSe by thermal quenching and hydrostatic high-pressure

We also examined the defects formed during the thermal quenching of Al_2O_3-capped GaSe with a thickness of 215 nm, as shown in Figure S4. Figure 3a shows the PL spectrum of annealed multilayer GaSe with a D peak near 1.93 eV, close to that produced through UV-325 nm irradiation in Figure 1, while the A peak is around 1.99 eV. Figure 3b shows the PL spectrum of the GaSe flake measured under 0.8 GPa, that resulted in a defect peak near 1.92 eV, while the A peak is around 1.97 eV. The shift of the free exciton peak is due to the strain effect.[64,65] For InSe, we generated defects through the same thermal annealing process in a 150 nm multilayer sample, as shown in Figure S5. The D peak shows up near 1.21 eV in Figure 3c, at the same location as that in the UV-irradiated sample in Figure 2. The PL spectra in Figure 3 shows that the defect-bound exciton emission (D peak) is not limited to UV irradiation but also appears after thermal annealing and high-pressure treatment. This comparison confirms that all three methods generate similar defect states, underscoring the common origin of the defect-related PL features observed in this study.

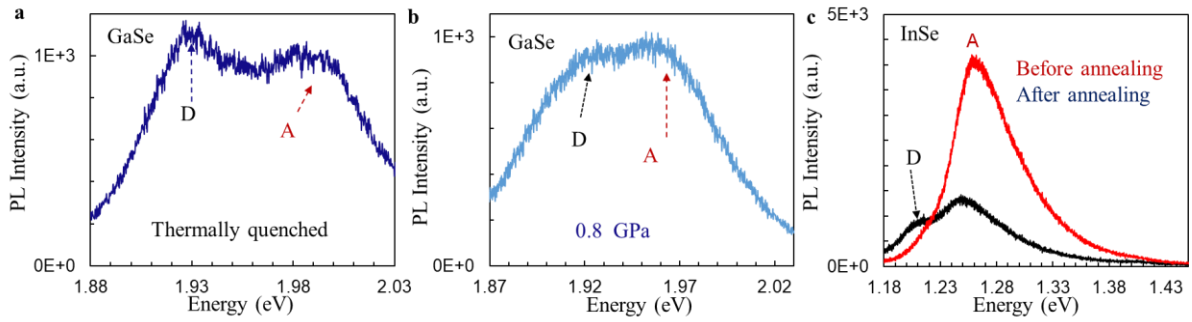

Figure 3: PL spectra from (a) air annealed multilayer GaSe, (b) GaSe after 0.8 GPa hydrostatic pressure treatment. (c) PL spectra before and after air annealing of multilayer InSe.

Grating pattern in Multilayer GaSe Protected by Al_2O_3

We test the capability of UV 325 nm laser writing of optical components in GaSe coated with 30 nm Al_2O_3. Figure S6 shows the optical setup for the two-beam interference for the generation of a grating pattern in multi-layer GaSe. The UV 325 nm laser passes through a beam splitter, and two beams are reflected by two mirrors and overlap on the GaSe sample with a thickness of 190 nm (Figure S7). We use the piezo stage in the fluorescence lifetime imaging microscopy (FLIM), where the PL intensity is shown by the event count scale while the average lifetime is shown by

the color scale, to record the grating patterns. The multilayer GaSe sample received UV-325 nm laser irradiation of two-beam interference (the overlapped beam size is 1.2 mm in diameter) for 30 min. The sample exhibits an A peak near 1.9 eV (623 nm) and a D peak near 1.86 eV (665 nm) as shown in Figure S8a. Thus, the (620 ± 5) nm and (650 ± 20) nm bandpass filters can cover the spectral region of the A and D peaks, respectively. As shown in Figure 4a, the two-beam UV treatment results in a grating pattern of periodic low-high lifetime events of the peak A. The dark regions have low lifetime events, indicating that those regions received a relatively high UV dose and were degraded. The green region not only has high lifetime events but also is almost uniform in lifetime. The center of the green lines is very bright and has the highest lifetime events. However, the grating pattern is barely visible in the FLIM in Figure 4b using the 650 nm bandpass filter for the defect emission line.

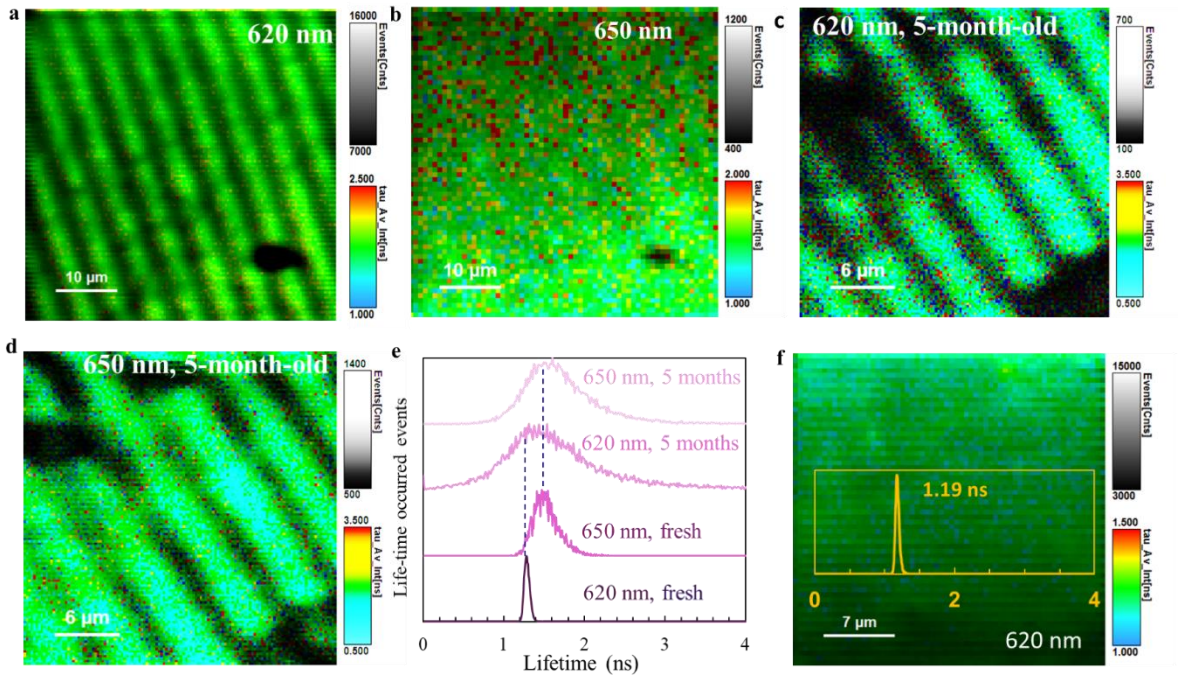

Figure 4: FLIM in UV irradiated multilayer GaSe: fresh sample using (a) 620±5 nm bandpass filter and (b) 650±20 nm bandpass filter. (c-e) 5-month-old sample using (c) the 620 nm filter, (d) 650 nm filter, and (e) their lifetime histograms. (f) FLIM using 620 nm filter from the GaSe without the UV exposure. The inset is its lifetime histogram centered at 1.19 ns.

We checked the stability of the grating pattern in GaSe. We measured PL and FLIM after the sample had been in the glove box for 5 months. The PL shown in Figure S8b exhibits a dominant D peak at 1.86 eV (665 nm) and a weaker A peak at 1.98 eV (620 nm), indicating preserved optical quality. Despite minor intensity variations relative to Figure S8a, the persistence of sharp D and A peaks after five months confirms stable radiative efficiency and minimal nonradiative degradation. Figure 4c and 4d show FLIMs using bandpass filters (620 ± 5) nm for the A peak emission and (650 ± 20) nm for the D peak, respectively. The PL lifetime in bright regions in Figure 4c is relatively uniform in light-blue color, with a peak around 1.48 ns as summarized in the lifetime histogram in Figure 4e. Red and dark-blue spots, corresponding to higher or lower lifetime than the light-blue, respectively, appear between the bright lines in Figure 4c. A similar FLIM pattern for defect emission in Figure 4d is observed as the one in Figure 4c, except that there are fewer red or dark-blue spots between the bright lines that have a cyan (blue-green) color. As a result, the lifetime histogram for the defect emission (using a 650 nm filter in Figure 4) is narrower, and the peak lifetime is larger than that for the free exciton emission (620 nm filter in Figure 4). Overall, the lifetime histogram in the freshly irradiated grating is broader compared to the uniform lifetime map of 1.19 ns in GaSe without UV exposure in Figure 4f. It becomes even broader when the sample is old. As observed in the FLIM in Figure 4, the defects within the region of low exciton emission intensity (i.e., high defect region) is not stable. The high defect emission region corresponds to the high free-exciton emission region in the aged grating pattern. It indicates that defect emissions intensity drops when the defect level goes above a certain threshold. Under strong laser exposure, excessive defect generation and local heating in the layered GaSe structure lead to stacking faults and dislocations, which act as non-radiative recombination centers and initially quench the defect-related emission. .[53] After aging, the local lattice gradually relaxes as the transient heat dissipates, and some irradiation-induced vacancies undergo partial healing through atom migration and recombination, as previously reported in atomically thin GaSe.[66] This relaxation and defect recovery reduce the non-radiative trap density below the quenching threshold. The remaining shallow defects, mainly selenium vacancies (V_{se}), act as radiative centers resulting in more stable emission. The observed high PL contrast between bright and dark regions in the grating confirms the excellent optical quality of the patterned structure, comparable to or exceeding those in other UV-inscribed polymer and 2D-material-based gratings.[67,68] These results

demonstrate the potential of the UV-writing technique in GaSe for scalable photonic device fabrication and wavelength-selective optical integration.

We measured the PL of the grating sample after 5 months, as shown in the supporting information Figure S8. Both A and D peaks become broader than those in the fresh sample, corresponding to the broad lifetime in the aged sample in the FLIM measurement.

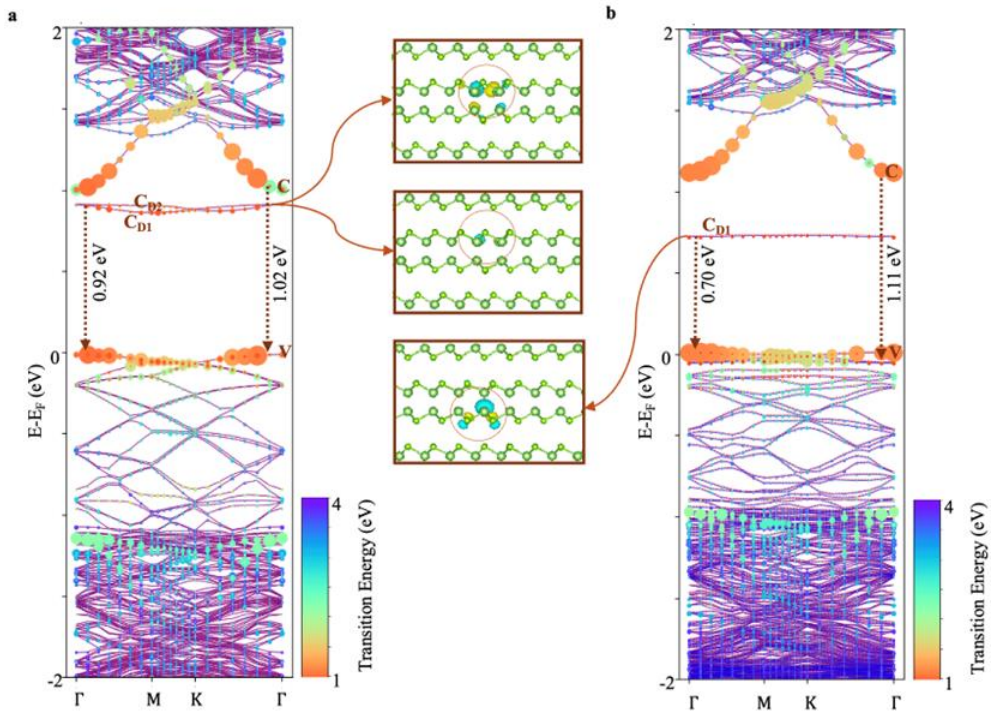

Figure 5: Band structures of (**a**) a V_{Se} and (**b**) a V_{Ga}, where optical transition matrix element magnitudes are overlayed on top (see main text). All energies referenced against the VBM. Circle sizes represent the magnitude of the transition matrix elements. Circles are color-coded according to transition energies. The three boxes in the middle show side views the localized wavefunctions of the respective defect states. The encircled region marks the location of the introduced point defect.

Calculated defect energies in GaSe

Ga or Se vacancy defects can be formed in GaSe.[66] A selenium vacancy is a prototypical defect model in GaSe due to its relatively low formation energy, as reported in a prior study.[69] To identify

the exact defect species using their spectroscopic signatures, we modeled the electronic structures of two prototypical defects in GaSe as candidates, all performed at the DFT level. We consider selenium and gallium vacancies, reported previously to have relatively small defect formation energies.[69,70] For both defects, we observed unoccupied mid-gap states, labeled as C_{D1} and C_{D2} for V_{Se} and only C_{D1} for V_{Ga}, as shown in Figure 5. The side view of the defect wavefunctions is shown to the right of the band structure in real space, confirming their localized nature. To determine the optical activity of interband transitions, on top of the band structure we overlay pairs of circles for all possible vertical transitions, where the color of the circle represents DFT energy intervals, and the circle diameter indicates the magnitude of the independent-particle optical transition matrix element along the in-plane direction (i.e. summing squared *xx* and *yy* components). A similar plot for pristine GaSe is provided in the supporting information Figures S9 and S10 for comparison. As seen from Figure 5, transition matrix elements in both cases are dominated by the interband transitions spanning over 1 eV (orange circles) involving pristine band edges (labeled V and C). The next most prominent transitions for both defect models are ones involving the pristine valence band edge state and the mid-gap states, colored in red. For V_{Se}, the $V \rightarrow C_{D1/2}$ transition is ~0.92 eV, which is close to the 1.10 eV as reported in a previous study.[69] The energy difference between this transition and the pristine band gap (1.07 eV obtained from a separate pristine structure calculation) is approximately 0.15 eV. This energy difference compares well with the experimentally measured peak position separation of 0.08-0.10 eV between the free exciton peak and defect-bound exciton peak. The same degree of agreement does not apply to V_{Ga}. For V_{Ga}, the $V \rightarrow C_{D1}$ transition is 0.70 eV. Here, the energy difference between this transition energy and the pristine GaSe band gap is 0.36 eV, which clearly disagrees with the experimentally measured peak energy difference. The above results allow us to conclude that the dominant defect species in our study is V_{Se}.

Conclusion:

In summary, we have shown that 325 nm UV laser can easily generate defects in both GaSe and InSe, and that it is much easier to generate defects in InSe which is much more prone to laser power-related degradation than in GaSe. The defects in GaSe and InSe with Al_2O_3 protection are stable. However, the defects in GaSe generated above a certain irradiation threshold are not stable in a sample that is five months old. We have generated a grating pattern of a low-high array of free

exciton emissions in multiple-layer GaSe. A similar grating pattern of a low-high array of defect emission has been observed in the aged GaSe sample. DFT has been calculated to identify the defect type. These results indicate that the 325 UV laser can be used to scribe photonic circuits in 2D layered GaSe for photonic integration.

Supporting Information:

Side-view schematic of multilayer γ-InSe/ε-GaSe phases, Raman spectrum, thickness profile, optical image, two-beam interference setup for generating periodic patterns on GaSe, PL spectrum, band structures plot.

Acknowledgments: S.K. and A.V.D. acknowledge support from the Material Genome Initiative funding allocated to NIST. J.C. and Y.L. acknowledge partial financial support from the U.S. National Science Foundation, grant number 2128367. Y.L. acknowledges partial financial support by the Department of Energy/National Nuclear Security Administration under Award Number DE-NA0004114. Y.W. acknowledges startup funds from UNT and partial support from NSF DMR-2340733.

Disclaimer:

The authors declare no conflict of interest. This report was prepared as an account of work sponsored by an agency of the United States Government. Neither the United States Government nor any agency thereof, nor any of their employees, makes any warranty, express or implied, or assumes any legal liability or responsibility for the accuracy, completeness, or usefulness of any information, apparatus, product, or process disclosed, or represents that its use would not infringe privately owned rights. Reference herein to any specific commercial product, process, or service by trade name, trademark, manufacturer, or otherwise does not necessarily constitute or imply its endorsement, recommendation, or favoring by the United States Government or any agency thereof. The views and opinions of authors expressed herein do not necessarily state or reflect those of the United States Government or any agency thereof.

References:

(1) Liu, H.; Neal, A. T.; Zhu, Z.; Luo, Z.; Xu, X.; Tománek, D.; Ye, P. D. Phosphorene: An Unexplored 2D Semiconductor with a High Hole Mobility. *ACS Nano* **2014**, *8* (4), 4033–4041. https://doi.org/10.1021/nn501226z.
(2) Li, L.; Yu, Y.; Ye, G. J.; Ge, Q.; Ou, X.; Wu, H.; Feng, D.; Chen, X. H.; Zhang, Y. Black Phosphorus Field-Effect Transistors. *Nat Nanotechnol* **2014**, *9* (5), 372–377. https://doi.org/10.1038/nnano.2014.35.
(3) Dai, M.; Gao, C.; Nie, Q.; Wang, Q.; Lin, Y.; Chu, J.; Li, W. Properties, Synthesis, and Device Applications of 2D Layered InSe. *Adv Mater Technol* **2022**, *7* (12), 1–31. https://doi.org/10.1002/admt.202200321.
(4) Wang, Q. H.; Kalantar-Zadeh, K.; Kis, A.; Coleman, J. N.; Strano, M. S. Electronics and Optoelectronics of Two-Dimensional Transition Metal Dichalcogenides. *Nat Nanotechnol* **2012**, *7* (11), 699–712. https://doi.org/10.1038/nnano.2012.193.
(5) Butler, S. Z.; Hollen, S. M.; Cao, L.; Cui, Y.; Gupta, J. A.; Gutiérrez, H. R.; Heinz, T. F.; Hong, S. S.; Huang, J.; Ismach, A. F.; Johnston-Halperin, E.; Kuno, M.; Plashnitsa, V. V.; Robinson, R. D.; Ruoff, R. S.; Salahuddin, S.; Shan, J.; Shi, L.; Spencer, M. G.; Terrones, M.; Windl, W.; Goldberger, J. E. Progress, Challenges, and Opportunities in Two-Dimensional Materials Beyond Graphene. *ACS Nano* **2013**, *7* (4), 2898–2926. https://doi.org/10.1021/nn400280c.
(6) Camara, M. O. D.; Mauger, A.; Devos, I. Electronic Structure of the Layer Compounds GaSe and InSe in a Tight-Binding Approach. *Phys Rev B* **2002**, *65* (12), 1–12. https://doi.org/10.1103/PhysRevB.65.125206.
(7) Li, M.; Lin, C.; Yang, S.; Chang, Y.; Chang, J.; Yang, F.; Zhong, C.; Jian, W.; Lien, C.; Ho, C.; Liu, H.; Huang, R.; Li, W.; Lin, Y.; Chu, J. High Mobilities in Layered InSe Transistors with Indium-Encapsulation-Induced Surface Charge Doping. *Advanced Materials* **2018**, *30* (44), 1–10. https://doi.org/10.1002/adma.201803690.
(8) Cai, H.; Gu, Y.; Lin, Y.-C.; Yu, Y.; Geohegan, D. B.; Xiao, K. Synthesis and Emerging Properties of 2D Layered III–VI Metal Chalcogenides. *Appl Phys Rev* **2019**, *6* (4), 1–30. https://doi.org/10.1063/1.5123487.
(9) Li, X.; Lin, M.-W.; Lin, J.; Huang, B.; Puretzky, A. A.; Ma, C.; Wang, K.; Zhou, W.; Pantelides, S. T.; Chi, M.; Kravchenko, I.; Fowlkes, J.; Rouleau, C. M.; Geohegan, D. B.; Xiao, K. Two-Dimensional GaSe/$MoSe_2$ Misfit Bilayer Heterojunctions by van Der Waals Epitaxy. *Sci Adv* **2016**, *2* (4), 1–10. https://doi.org/10.1126/sciadv.1501882.
(10) Mudd, G. W.; Svatek, S. A.; Ren, T.; Patanè, A.; Makarovsky, O.; Eaves, L.; Beton, P. H.; Kovalyuk, Z. D.; Lashkarev, G. V.; Kudrynskyi, Z. R.; Dmitriev, A. I. Tuning the Bandgap of Exfoliated InSe Nanosheets by Quantum Confinement. *Advanced Materials* **2013**, *25* (40), 5714–5718. https://doi.org/10.1002/adma.201302616.
(11) Rybkovskiy, D. V.; Osadchy, A. V.; Obraztsova, E. D. Transition from Parabolic to Ring-Shaped Valence Band Maximum in Few-Layer GaS, GaSe, and InSe. *Phys Rev B* **2014**, *90* (23), 235302(1)-235302(9). https://doi.org/10.1103/PhysRevB.90.235302.
(12) Magorrian, S. J.; Zólyomi, V.; Fal'ko, V. I. Spin-Orbit Coupling, Optical Transitions, and Spin Pumping in Monolayer and Few-Layer InSe. *Phys Rev B* **2017**, *96* (19), 1–6. https://doi.org/10.1103/PhysRevB.96.195428.
(13) Ceferino, A.; Magorrian, S. J.; Zólyomi, V.; Bandurin, D. A.; Geim, A. K.; Patanè, A.; Kovalyuk, Z. D.; Kudrynskyi, Z. R.; Grigorieva, I. V.; Fal'ko, V. I. Tunable Spin-Orbit

Coupling in Two-Dimensional InSe. *Phys Rev B* **2021**, *104* (12), 1–21. https://doi.org/10.1103/PhysRevB.104.125432.
(14) Bandurin, D. A.; Tyurnina, A. V.; Yu, G. L.; Mishchenko, A.; Zólyomi, V.; Morozov, S. V.; Kumar, R. K.; Gorbachev, R. V.; Kudrynskyi, Z. R.; Pezzini, S.; Kovalyuk, Z. D.; Zeitler, U.; Novoselov, K. S.; Patanè, A.; Eaves, L.; Grigorieva, I. V.; Fal'ko, V. I.; Geim, A. K.; Cao, Y. High Electron Mobility, Quantum Hall Effect and Anomalous Optical Response in Atomically Thin InSe. *Nat Nanotechnol* **2017**, *12* (3), 223–227. https://doi.org/10.1038/nnano.2016.242.
(15) Mudd, G. W.; Molas, M. R.; Chen, X.; Zólyomi, V.; Nogajewski, K.; Kudrynskyi, Z. R.; Kovalyuk, Z. D.; Yusa, G.; Makarovsky, O.; Eaves, L.; Potemski, M.; Fal'ko, V. I.; Patanè, A. The Direct-to-Indirect Band Gap Crossover in Two-Dimensional van Der Waals Indium Selenide Crystals. *Sci Rep* **2016**, *6* (1), 1–10. https://doi.org/10.1038/srep39619.
(16) Hu, P.; Wen, Z.; Wang, L.; Tan, P.; Xiao, K. Synthesis of Few-Layer GaSe Nanosheets for High Performance Photodetectors. *ACS Nano* **2012**, *6* (7), 5988–5994. https://doi.org/10.1021/nn300889c.
(17) Rybkovskiy, D. V.; Arutyunyan, N. R.; Orekhov, A. S.; Gromchenko, I. A.; Vorobiev, I. V.; Osadchy, A. V.; Salaev, E. Yu.; Baykara, T. K.; Allakhverdiev, K. R.; Obraztsova, E. D. Size-Induced Effects in Gallium Selenide Electronic Structure: The Influence of Interlayer Interactions. *Phys Rev B* **2011**, *84* (8), 1–7. https://doi.org/10.1103/PhysRevB.84.085314.
(18) Chuang, C.-A.; Lin, M.-H.; Yeh, B.-X.; Ho, C.-H. Curvature-Dependent Flexible Light Emission from Layered Gallium Selenide Crystals. *RSC Adv* **2018**, *8* (5), 2733–2739. https://doi.org/10.1039/C7RA11600D.
(19) Zhao, Q.; Frisenda, R.; Wang, T.; Castellanos-Gomez, A. InSe: A Two-Dimensional Semiconductor with Superior Flexibility. *Nanoscale* **2019**, *11* (20), 9845–9850. https://doi.org/10.1039/C9NR02172H.
(20) Tonndorf, P.; Schwarz, S.; Kern, J.; Niehues, I.; Del Pozo-Zamudio, O.; Dmitriev, A. I.; Bakhtinov, A. P.; Borisenko, D. N.; Kolesnikov, N. N.; Tartakovskii, A. I.; Michaelis de Vasconcellos, S.; Bratschitsch, R. Single-Photon Emitters in GaSe. *2d Mater* **2017**, *4* (2), 1–6. https://doi.org/10.1088/2053-1583/aa525b.
(21) Shi, W.; Ding, Y. J. A Monochromatic and High-Power Terahertz Source Tunable in the Ranges of 2.7–38.4 and 58.2–3540 Mm for Variety of Potential Applications. *Appl Phys Lett* **2004**, *84* (10), 1635–1637. https://doi.org/10.1063/1.1649802.
(22) Jie, W.; Chen, X.; Li, D.; Xie, L.; Hui, Y. Y.; Lau, S. P.; Cui, X.; Hao, J. Layer-Dependent Nonlinear Optical Properties and Stability of Non-Centrosymmetric Modification in Few-Layer GaSe Sheets. *Angewandte Chemie International Edition* **2015**, *54* (4), 1185–1189. https://doi.org/10.1002/anie.201409837.
(23) Liu, K.; Xu, J.; Zhang, X.-C. GaSe Crystals for Broadband Terahertz Wave Detection. *Appl Phys Lett* **2004**, *85* (6), 863–865. https://doi.org/10.1063/1.1779959.
(24) Zahner, S.; Kador, L.; Allakhverdiev, K. R.; Salaev, E. Yu.; Huseyinoğlu, M. F. Fluorescence Lifetime Imaging Microscopy and Polar-Plot Analysis of Gallium Selenide Crystals. *J Appl Phys* **2014**, *115* (4), 1–7. https://doi.org/10.1063/1.4862852.

(25) Luo, W.; Cao, Y.; Hu, P.; Cai, K.; Feng, Q.; Yan, F.; Yan, T.; Zhang, X.; Wang, K. Gate Tuning of High-Performance InSe-Based Photodetectors Using Graphene Electrodes. *Adv Opt Mater* **2015**, *3* (10), 1418–1423. https://doi.org/10.1002/adom.201500190.
(26) Chen, L.; Yu, Z. G.; Liang, D.; Li, S.; Tan, W. C.; Zhang, Y.-W.; Ang, K.-W. Ultrasensitive and Robust Two-Dimensional Indium Selenide Flexible Electronics and Sensors for Human Motion Detection. *Nano Energy* **2020**, *76*, 1–10. https://doi.org/10.1016/j.nanoen.2020.105020.
(27) Tang, Y.; Lei, P.; Liao, K.; Jiang, T.; Chen, S.; Xie, Q.; Luo, W.; Zhao, Y.; Jie, W. Observation of Nonvolatile Resistive Switching Behaviors in 2D Layered InSe Nanosheets through Controllable Oxidation. *Appl Phys Lett* **2021**, *119* (13), 1–6. https://doi.org/10.1063/5.0061792.
(28) Song, C.; Huang, S.; Wang, C.; Luo, J.; Yan, H. The Optical Properties of Few-Layer InSe. *J Appl Phys* **2020**, *128* (6), 1–20. https://doi.org/10.1063/5.0018480.
(29) Zuo, Y.; Antonatos, N.; Děkanovský, L.; Luxa, J.; Elliott, J. D.; Gianolio, D.; Šturala, J.; Guzzetta, F.; Mourdikoudis, S.; Regner, J.; Málek, R.; Sofer, Z. Defect Engineering in Two-Dimensional Layered $PdTe_2$ for Enhanced Hydrogen Evolution Reaction. *ACS Catal* **2023**, *13* (4), 2601–2609. https://doi.org/10.1021/acscatal.2c04968.
(30) Abidi, I. H.; Giridhar, S. P.; Tollerud, J. O.; Limb, J.; Waqar, M.; Mazumder, A.; Mayes, E. L.; Murdoch, B. J.; Xu, C.; Bhoriya, A.; Ranjan, A.; Ahmed, T.; Li, Y.; Davis, J. A.; Bentley, C. L.; Russo, S. P.; Gaspera, E. Della; Walia, S. Oxygen Driven Defect Engineering of Monolayer MoS_2 for Tunable Electronic, Optoelectronic, and Electrochemical Devices. *Adv Funct Mater* **2024**, *34* (37), 1–11. https://doi.org/10.1002/adfm.202402402.
(31) Jo, J.; Kim, J. H.; Kim, C. H.; Lee, J.; Choe, D.; Oh, I.; Lee, S.; Lee, Z.; Jin, H.; Yoo, J.-W. Defect-Gradient-Induced Rashba Effect in van Der Waals PtSe2 Layers. *Nat Commun* **2022**, *13* (1), 1–8. https://doi.org/10.1038/s41467-022-30414-4.
(32) Santra, P.; Ghaderzadeh, S.; Ghorbani-Asl, M.; Komsa, H.-P.; Besley, E.; Krasheninnikov, A. V. Strain-Modulated Defect Engineering of Two-Dimensional Materials. *NPJ 2D Mater Appl* **2024**, *8* (1), 1–9. https://doi.org/10.1038/s41699-024-00472-x.
(33) Mitterreiter, E.; Schuler, B.; Micevic, A.; Hernangómez-Pérez, D.; Barthelmi, K.; Cochrane, K. A.; Kiemle, J.; Sigger, F.; Klein, J.; Wong, E.; Barnard, E. S.; Watanabe, K.; Taniguchi, T.; Lorke, M.; Jahnke, F.; Finley, J. J.; Schwartzberg, A. M.; Qiu, D. Y.; Refaely-Abramson, S.; Holleitner, A. W.; Weber-Bargioni, A.; Kastl, C. The Role of Chalcogen Vacancies for Atomic Defect Emission in MoS2. *Nat Commun* **2021**, *12* (1), 1–8. https://doi.org/10.1038/s41467-021-24102-y.
(34) Luo, W.; Lawrie, B. J.; Puretzky, A. A.; Tan, Q.; Gao, H.; Lingerfelt, D. B.; Eichman, G.; Mcgee, E.; Swan, A. K.; Liang, L.; Ling, X. Imaging Strain-Localized Single-Photon Emitters in Layered GaSe below the Diffraction Limit. *ACS Nano* **2023**, *17* (23), 23455–23465. https://doi.org/10.1021/acsnano.3c05250.
(35) Zhao, H.; Hus, S. M.; Chen, J.; Yan, X.; Lawrie, B. J.; Jesse, S.; Li, A.-P.; Liang, L.; Htoon, H. Telecom-Wavelength Single-Photon Emitters in Multilayer InSe. *ACS Nano* **2025**, *19* (7), 6911–6917. https://doi.org/10.1021/acsnano.4c13888.

(36) McMillen, B.; Jewart, C.; Buric, M.; Chen, K. P.; Lin, Y.; Xu, W. Fiber Bragg Grating Vacuum Sensors. *Appl Phys Lett* **2005**, *87* (23), 1–3. https://doi.org/10.1063/1.2140082.
(37) Wu, C.; Deng, H.; Huang, Y.-S.; Yu, H.; Takeuchi, I.; Ríos Ocampo, C. A.; Li, M. Freeform Direct-Write and Rewritable Photonic Integrated Circuits in Phase-Change Thin Films. *Sci Adv* **2024**, *10* (1), 1–7. https://doi.org/10.1126/sciadv.adk1361.
(38) Ocier, C. R.; Richards, C. A.; Bacon-Brown, D. A.; Ding, Q.; Kumar, R.; Garcia, T. J.; van de Groep, J.; Song, J.-H.; Cyphersmith, A. J.; Rhode, A.; Perry, A. N.; Littlefield, A. J.; Zhu, J.; Xie, D.; Gao, H.; Messinger, J. F.; Brongersma, M. L.; Toussaint, K. C.; Goddard, L. L.; Braun, P. V. Direct Laser Writing of Volumetric Gradient Index Lenses and Waveguides. *Light Sci Appl* **2020**, *9* (1), 1–14. https://doi.org/10.1038/s41377-020-00431-3.
(39) Wang, X.-J.; Fang, H.-H.; Li, Z.-Z.; Wang, D.; Sun, H.-B. Laser Manufacturing of Spatial Resolution Approaching Quantum Limit. *Light Sci Appl* **2024**, *13* (1), 1–8. https://doi.org/10.1038/s41377-023-01354-5.
(40) Wang, W.; Jones, L. O.; Chen, J.-S.; Schatz, G. C.; Ma, X. Utilizing Ultraviolet Photons to Generate Single-Photon Emitters in Semiconductor Monolayers. *ACS Nano* **2022**, *16* (12), 21240–21247. https://doi.org/10.1021/acsnano.2c09209.
(41) Varghese, S.; Hurley, N.; Kamau, S.; Jiang, Y.; Rodriguez, R. G.; Bhandari, B.; Lyu, T.; Yan, H.; Wang, Y.; Kaul, A. B.; Cui, J.; Lin, Y. Thermal-Strain-Enabled Enhanced Emission from UV Laser-Induced Defect Levels near the Surface of Multilayer MoS_2. *ACS Applied Optical Materials* **2024**, *2* (8), 1721–1729. https://doi.org/10.1021/acsaom.4c00276.
(42) Varghese, S.; Wang, S.; Neupane, B.; Bhandari, B.; Jiang, Y.; Gonzalez Rodriguez, R.; Krylyuk, S.; Davydov, A. V.; Yan, H.; Wang, Y.; Kaul, A. B.; Cui, J.; Lin, Y. Quantum Emitters Induced by High Pressure and UV Laser Irradiation in Multilayer GaSe. *ACS Omega* **2025**, *10* (7), 7466–7473. https://doi.org/10.1021/acsomega.5c00680.
(43) Bessonov, A. A.; Kirikova, M. N.; Petukhov, D. I.; Allen, M.; Ryhänen, T.; Bailey, M. J. A. Layered Memristive and Memcapacitive Switches for Printable Electronics. *Nat Mater* **2015**, *14* (2), 199–204. https://doi.org/10.1038/nmat4135.
(44) Perdew, J. P.; Burke, K.; Ernzerhof, M. Generalized Gradient Approximation Made Simple. *Phys Rev Lett* **1996**, *77* (18), 3865–3868. https://doi.org/10.1103/PhysRevLett.77.3865.
(45) Kresse, G.; Furthmüller, J. Efficiency of Ab-Initio Total Energy Calculations for Metals and Semiconductors Using a Plane-Wave Basis Set. *Comput Mater Sci* **1996**, *6* (1), 15–50. https://doi.org/10.1016/0927-0256(96)00008-0.
(46) Kresse, G.; Furthmüller, J. Efficient Iterative Schemes for *Ab Initio* Total-Energy Calculations Using a Plane-Wave Basis Set. *Phys Rev B* **1996**, *54* (16), 11169–11186. https://doi.org/10.1103/PhysRevB.54.11169.
(47) Kresse, G.; Joubert, D. From Ultrasoft Pseudopotentials to the Projector Augmented-Wave Method. *Phys Rev B* **1999**, *59* (3), 1758–1775. https://doi.org/10.1103/PhysRevB.59.1758.
(48) Blöchl, P. E. Projector Augmented-Wave Method. *Phys Rev B* **1994**, *50* (24), 17953–17979. https://doi.org/10.1103/PhysRevB.50.17953.

(49) Lang, L.; Tavadze, P.; Tellez, A.; Bousquet, E.; Xu, H.; Muñoz, F.; Vasquez, N.; Herath, U.; Romero, A. H. Expanding PyProcar for New Features, Maintainability, and Reliability. *Comput Phys Commun* **2024**, *297*, 1–18. https://doi.org/10.1016/j.cpc.2023.109063.

(50) Herath, U.; Tavadze, P.; He, X.; Bousquet, E.; Singh, S.; Muñoz, F.; Romero, A. H. PyProcar: A Python Library for Electronic Structure Pre/Post-Processing. *Comput Phys Commun* **2020**, *251*, 1–14. https://doi.org/10.1016/j.cpc.2019.107080.

(51) Hunter, J. D. Matplotlib: A 2D Graphics Environment. *Comput Sci Eng* **2007**, *9* (3), 90–95. https://doi.org/10.1109/MCSE.2007.55.

(52) Molas, M. R.; Tyurnina, A. V.; Zólyomi, V.; Ott, A. K.; Terry, D. J.; Hamer, M. J.; Yelgel, C.; Babiński, A.; Nasibulin, A. G.; Ferrari, A. C.; Fal'ko, V. I.; Gorbachev, R. Raman Spectroscopy of GaSe and InSe Post-Transition Metal Chalcogenides Layers. *Faraday Discuss* **2021**, *227*, 163–170. https://doi.org/10.1039/D0FD00007H.

(53) Wei, C.; Chen, X.; Li, D.; Su, H.; He, H.; Dai, J.-F. Bound Exciton and Free Exciton States in GaSe Thin Slab. *Sci Rep* **2016**, *6* (1), 1–6. https://doi.org/10.1038/srep33890.

(54) Pozo-Zamudio, O. Del; Schwarz, S.; Sich, M.; Akimov, I. A.; Bayer, M.; Schofield, R. C.; Chekhovich, E. A.; Robinson, B. J.; Kay, N. D.; Kolosov, O. V; A I Dmitriev; Lashkarev, G. V; Borisenko, D. N.; Kolesnikov, N. N.; Tartakovskii, A. I. Photoluminescence of Two-Dimensional GaTe and GaSe Films. *2d Mater* **2015**, *2* (3), 1–9. https://doi.org/10.1088/2053-1583/2/3/035010.

(55) Usman, M.; Golovynskyi, S.; Dong, D.; Lin, Y.; Yue, Z.; Imran, M.; Li, B.; Wu, H.; Wang, L. Raman Scattering and Exciton Photoluminescence in Few-Layer GaSe: Thickness- and Temperature-Dependent Behaviors. *The Journal of Physical Chemistry C* **2022**, *126* (25), 10459–10468. https://doi.org/10.1021/acs.jpcc.2c02127.

(56) Schmeink, J.; Osterfeld, J.; Kharsah, O.; Sleziona, S.; Schleberger, M. Unraveling the Influence of Defects in Janus MoSSe and Janus Alloys MoS2(1−x)Se2x. *NPJ 2D Mater Appl* **2024**, *8* (1), 1–10. https://doi.org/10.1038/s41699-024-00504-6.

(57) Varghese, S.; Neupane, B.; Bhandari, B.; Wang, S.; Jiang, Y.; Gonzalez Rodriguez, R.; Krylyuk, S.; Davydov, A. V.; Wang, Y.; Yan, H.; Kaul, A.; Cui, J.; Lin, Y. Strain-Modulated Exciton Localization and Enhanced Emission in Multilayer GaSe. *The Journal of Physical Chemistry C* **2025**, *129* (30), 13638–13647. https://doi.org/10.1021/acs.jpcc.5c02229.

(58) Wang, J.; Yue, X.; Zhu, J.; Hu, L.; Liu, R.; Cong, C.; Qiu, Z.-J. Revealing the Origin of PL Evolution of InSe Flake Induced by Laser Irradiation. *RSC Adv* **2023**, *13* (12), 7780–7788. https://doi.org/10.1039/D3RA00324H.

(59) He, Z.; Xu, W.; Zhou, Y.; Wang, X.; Sheng, Y.; Rong, Y.; Guo, S.; Zhang, J.; Smith, J. M.; Warner, J. H. Biexciton Formation in Bilayer Tungsten Disulfide. *ACS Nano* **2016**, *10* (2), 2176–2183. https://doi.org/10.1021/acsnano.5b06678.

(60) Carozo, V.; Wang, Y.; Fujisawa, K.; Carvalho, B. R.; McCreary, A.; Feng, S.; Lin, Z.; Zhou, C.; Perea-López, N.; Elías, A. L.; Kabius, B.; Crespi, V. H.; Terrones, M. Optical Identification of Sulfur Vacancies: Bound Excitons at the Edges of Monolayer Tungsten Disulfide. *Sci Adv* **2017**, *3* (4), 1–9. https://doi.org/10.1126/sciadv.1602813.

(61) Shang, J.; Shen, X.; Cong, C.; Peimyoo, N.; Cao, B.; Eginligil, M.; Yu, T. Observation of Excitonic Fine Structure in a 2D Transition-Metal Dichalcogenide Semiconductor. *ACS Nano* **2015**, *9* (1), 647–655. https://doi.org/10.1021/nn5059908.

(62) Kaplan, D.; Gong, Y.; Mills, K.; Swaminathan, V.; Ajayan, P. M.; Shirodkar, S.; Kaxiras, E. Excitation Intensity Dependence of Photoluminescence from Monolayers of MoS_2 and WS_2 /MoS_2 Heterostructures. *2d Mater* **2016**, *3* (1), 1–10. https://doi.org/10.1088/2053-1583/3/1/015005.

(63) Xie, Q.; Hu, C.; Xu, L.; Chen, L.; Wang, W.; Yin, H.; Cheng, G.; Ai, X. Stability Studies of Few-Layer InSe Nanosheets by Raman Spectroscopy. *Solid State Commun* **2021**, *336*, 114417. https://doi.org/10.1016/j.ssc.2021.114417.

(64) Lin, Y.; Hathaway, E.; Habis, F.; Wang, Y.; Rodriguez, R. G.; Alnasser, K.; Hurley, N.; Cui, J. Enhanced Emission from Defect Levels in Multilayer MoS_2. *Adv Opt Mater* **2022**, *10* (19), 1–9. https://doi.org/10.1002/adom.202201059.

(65) Lin, Y.; Hurley, N.; Kamau, S.; Hathaway, E.; Jiang, Y.; Rodriguez, R. G.; Varghese, S.; Krylyuk, S.; Davydov, A. V.; Wang, Y.; Kaul, A.; Cui, J. Strain-Activated Stimulated Emission from Multilayer $MoSe_2$ in a Narrow Operation Window. *physica status solidi (RRL) – Rapid Research Letters* **2023**, 1–8. https://doi.org/10.1002/pssr.202300343.

(66) Hopkinson, D. G.; Zólyomi, V.; Rooney, A. P.; Clark, N.; Terry, D. J.; Hamer, M.; Lewis, D. J.; Allen, C. S.; Kirkland, A. I.; Andreev, Y.; Kudrynskyi, Z.; Kovalyuk, Z.; Patanè, A.; Fal'ko, V. I.; Gorbachev, R.; Haigh, S. J. Formation and Healing of Defects in Atomically Thin GaSe and InSe. *ACS Nano* **2019**, *13* (5), 5112–5123. https://doi.org/10.1021/acsnano.8b08253.

(67) Yang, J.; Wang, Z.; Wang, F.; Xu, R.; Tao, J.; Zhang, S.; Qin, Q.; Luther-Davies, B.; Jagadish, C.; Yu, Z.; Lu, Y. Atomically Thin Optical Lenses and Gratings. *Light Sci Appl* **2016**, *5* (3), 1–8. https://doi.org/10.1038/lsa.2016.46.

(68) Kollipara, P. S.; Li, J.; Zheng, Y. Optical Patterning of Two-Dimensional Materials. *Research* **2020**, *2020*, 1–15. https://doi.org/10.34133/2020/6581250.

(69) Deák, P.; Han, M.; Lorke, M.; Tabriz, M. F.; Frauenheim, T. Intrinsic Defects of GaSe. *Journal of Physics Condensed Matter* **2020**, *32* (28), 1–5. https://doi.org/10.1088/1361-648X/ab7fdb.

(70) Bradford, J.; Rahman, K.; Felton, J.; Cheng, T. S.; Shiffa, M.; Beton, P. H.; Saywell, A.; Greenaway, M. T.; Novikov, S. V; O'Shea, J. N.; Patanè, A. Defect-Induced Doping and Chemisorption of O_2 in Se Deficient GaSe Monolayers. *2d Mater* **2025**, *12* (1), 1–9. https://doi.org/10.1088/2053-1583/ad9d57.

TOC

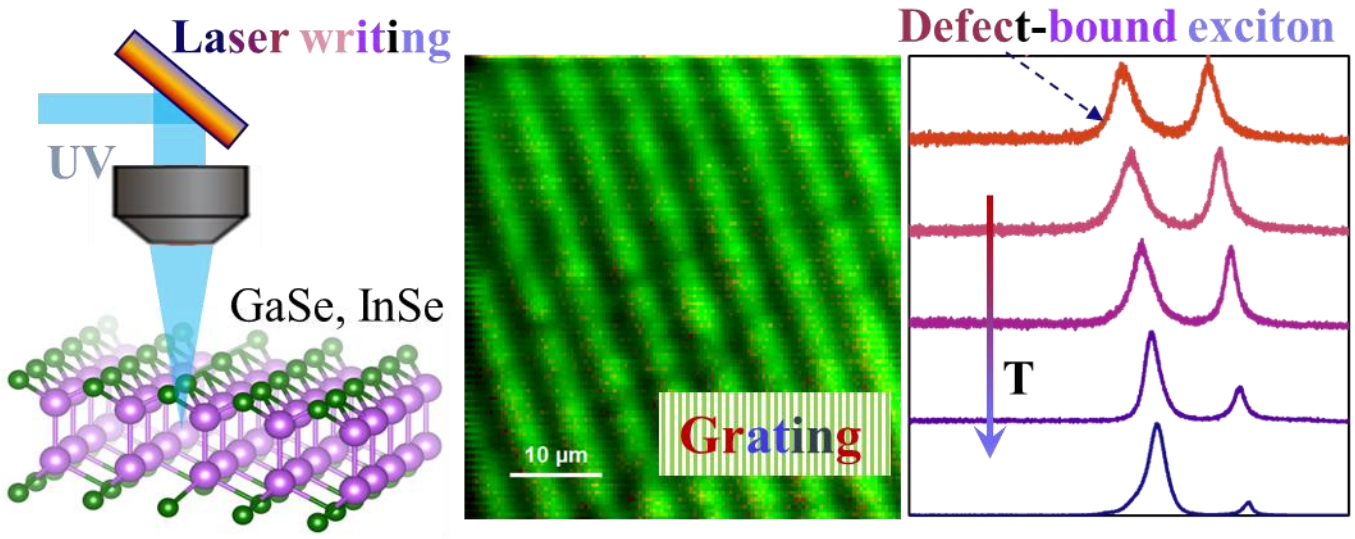
Laser writing
UV
GaSe, InSe
10 μm
Grating
Defect-bound exciton
T